AFRL-RX-WP-TP-2009-4096

A COMBINED EXPERIMENTAL AND COMPUTATIONAL STUDY TO EXAMINE LATERAL CONSTRAINT EFFECTS ON SINGLE-SLIP ORIENTED MICROCOMPRESSION EXPERIMENTS (PREPRINT)

M.D. Uchic, D.M. Dimiduk, H.L. Fraser, P.A. Shade, R. Wheeler, and Y.S. Choi

Metals Branch
Metals, Ceramics and NDE Division

APRIL 2009

AIR FORCE RESEARCH LABORATORY
MATERIALS AND MANUFACTURING DIRECTORATE
WRIGHT-PATTERSON AIR FORCE BASE, OH 45433-7750
AIR FORCE MATERIEL COMMAND
UNITED STATES AIR FORCE

REPORT DOCUMENTATION PAGE

Form Approved
OMB No. 0704-0188

1. REPORT DATE *(DD-MM-YY)*	2. REPORT TYPE	3. DATES COVERED *(From - To)*
April 2009	Journal Article Preprint	01 April 2009- 01 April 2009

4. TITLE AND SUBTITLE
A COMBINED EXPERIMENTAL AND COMPUTATIONAL STUDY TO EXAMINE LATERAL CONSTRAINT EFFECTS ON SINGLE-SLIP ORIENTED MICROCOMPRESSION EXPERIMENTS (PREPRINT)

5a. CONTRACT NUMBER
In-house

5b. GRANT NUMBER

5c. PROGRAM ELEMENT NUMBER
62102F

6. AUTHOR(S)
M.D. Uchic, D.M. Dimiduk, and H.L. Fraser (AFRL/RXLMD)
P.A. Shade (Ohio State University)
R. Wheeler and Y.S. Choi (UES, Inc.)

5d. PROJECT NUMBER
4347

5e. TASK NUMBER
RG

5f. WORK UNIT NUMBER
M02R1000

7. PERFORMING ORGANIZATION NAME(S) AND ADDRESS(ES)

Metals Branch (RXLMP)
Metals, Ceramics and NDE Division
Materials and Manufacturing Directorate
Wright-Patterson Air Force Base, OH 45433-7750
Air Force Materiel Command, United States Air Force

Ohio State University
Columbus, OH 43210

UES, Inc.
Dayton, OH 45432

8. PERFORMING ORGANIZATION REPORT NUMBER
AFRL-RX-WP-TP-2009-4096

9. SPONSORING/MONITORING AGENCY NAME(S) AND ADDRESS(ES)
Air Force Research Laboratory
Materials and Manufacturing Directorate
Wright-Patterson Air Force Base, OH 45433-7750
Air Force Materiel Command
United States Air Force

10. SPONSORING/MONITORING AGENCY ACRONYM(S)
AFRL/RXLMD

11. SPONSORING/MONITORING AGENCY REPORT NUMBER(S)
AFRL-RX-WP-TP-2009-4096

12. DISTRIBUTION/AVAILABILITY STATEMENT
Approved for public release; distribution unlimited.

13. SUPPLEMENTARY NOTES
To be submitted to Acta Materialia
PAO Case Number and clearance date: 88ABW-2008-1093, 24 November 2008.
The U.S. Government is joint author of this work and has the right to use, modify, reproduce, release, perform, display, or disclose the work.

14. ABSTRACT
A custom in-situ SEM mechanical testing system has been used to study the compressive deformation behavior of single-slip oriented Rene N5 microcrystals. Two different compression platens were used to explore the effect of lateral stiffness on the resultant mechanical response, which approximated either a full-frictional or zero-friction case. The change in the lateral constraint of the test system had a demonstrable effect on many aspects or attributes of plastic flow: the measured modulus, yield stress and strain hardening behavior, the intermittency of strain bursts, the spatial distribution of slip bands, and the development of internal lattice rotations. Finite element modeling of the microcompression experiments using a crystal plasticity framework enabled insight regarding changes in the internal stress field and resultant slip system activity. The experimental tests findings are rationalized based on these simulation results.

15. SUBJECT TERMS
in-situ SEM mechanical testing system, Rene N5, finite element modeling, crystal plasticity

16. SECURITY CLASSIFICATION OF:			17. LIMITATION OF ABSTRACT:	18. NUMBER OF PAGES	19a. NAME OF RESPONSIBLE PERSON (Monitor)
a. REPORT	b. ABSTRACT	c. THIS PAGE			Christopher F. Woodward
Unclassified	Unclassified	Unclassified	SAR	22	19b. TELEPHONE NUMBER *(Include Area Code)* N/A

Standard Form 298 (Rev. 8-98)
Prescribed by ANSI Std. Z39-18

A Combined Experimental and Computational Study to Examine Lateral Constraint Effects on Single-Slip Oriented Microcompression Experiments

P.A. Shade [a], R. Wheeler [b], Y.S. Choi [b], M.D. Uchic [c], D.M. Dimiduk [c], H.L Fraser [a]

[a] Department of Materials Science and Engineering, The Ohio State University, 477 Watts Hall, 2041 College Road, Columbus, OH 43210, USA
[b] UES Inc., 4401 Dayton-Xenia Road, Dayton, OH 45432, USA
[c] Air Force Research Laboratory, Materials and Manufacturing Directorate, 2230 10th Street, Wright-Patterson AFB, OH 45433, USA

Abstract

A custom in-situ SEM mechanical testing system has been used to study the compressive deformation behavior of single-slip oriented Rene N5 microcrystals. Two different compression platens were used to explore the effect of lateral stiffness on the resultant mechanical response, which approximated either a full-frictional or zero-friction case. The change in the lateral constraint of the test system had a demonstrable effect on many aspects or attributes of plastic flow: the measured modulus, yield stress and strain hardening behavior, the intermittency of strain bursts, the spatial distribution of slip bands, and the development of internal lattice rotations. Finite element modeling of the microcompression experiments using a crystal plasticity framework enabled insight regarding changes in the internal stress field and resultant slip system activity. The experimental tests findings are rationalized based on these simulation results.

1. Introduction

Seven years ago, some of the present authors developed a test methodology for measuring the flow behavior of miniature samples in compression [1]. The methodology consisted of fabricating micrometer-scale cylindrical samples using focused ion beam (FIB) milling and subsequently testing these in uniaxial compression with a commercial nanoindentation system outfitted with a flat punch [1,2]. Subsequent studies have applied various adaptations of the technique to study flow behavior in a variety of material systems [3-14]. Motivations for testing at this scale include the exploration of fundamental deformation micromechanisms, and the desire to sample local changes in mechanical properties due to microstructural variations.

As a logical extension of the aforementioned microcompression testing methodology, we have constructed a custom device for performing uniaxial mechanical tests on micrometer-scale specimens that can operate inside a scanning electron microscope (SEM) [15]. This device enables access to both tensile and compressive test modes, and also facilitates the direct observation of the spatial and temporal distribution of deformation events through continuous recording of SEM images. During the initial development of this device, we immediately recognized that the loading platen and the top surface of the microcompression sample moved as a single conjoined unit throughout

a test, unlike a macro-scale compression experiment where the sample slides against the compression platens. The lower end of the microcompression sample is integrally-connected to the substrate, and therefore the constraint imposed by the lateral stiffness of the loading platen significantly influences the resultant mechanical behavior. This constraint has a similar effect to that of friction at the platen-sample interface on macro-scale compression experiments.

The influence of platen-sample friction for macro-scale compression tests has been well known for a long time. Taylor and Farren [16] conducted compression experiments on single crystals of aluminum in 1926 and demonstrated that the use of a lubricant resulted in an increase in the uniformity of both the stress and strain distributions, as well as minimized the development of barreling in the test sample. Today, lubricants are commonly used to minimize friction in macro-scale compression testing [17]. Recently, considerable efforts have been undertaken by Lassila et al. [18,19] to construct a device capable of deforming single crystals in compression in the absence of frictional and rotational constraints.

In the case of microcompression experiments, applying a lubricant to the platen-sample interface represents a technical challenge. Alternatively, some of the present authors postulated that ease of translation of the loading axis in certain commercial nanoindentation systems allows the microcompression test to become effectively a low friction experiment [3]. Note that low friction experiments also have selected disadvantages, as Zhang et al. [20] and Raabe et al. [21] have used isotropic continuum finite element modeling (FEM) and anisotropic crystal plasticity FEM respectively to demonstrate a greater plastic buckling instability with decreasing platen-sample friction coefficient.

In this article, we show that the degree of lateral constraint imposed by the loading platen in microcompression experiments influences the measured modulus, yield stress and strain hardening behavior, the intermittency of strain bursts, the spatial distribution of slip bands, and the development of internal lattice rotations. Kiener et al. [22] and Maass et al. [23] used electron backscatter diffraction (EBSD) and Laue X-ray diffraction respectively to monitor lattice rotations developed in microcompression experiments on Cu. They observed disorientations of 5° or more in certain locations of the deformed specimen relative to the initial orientation. In contrast, Budiman et al. [24] used Laue X-ray diffraction to characterize a deformed Au microcompression specimen and found no evidence of lattice rotations. Additionally, the stress-strain curves of Kiener and Maass [22,23] show a higher degree of strain hardening than that in Budiman [24]. In light of the present work, this variation in observations may be due to differences in constraints imposed by the particular mechanical test system implemented in each study.

In this article, we highlight the effect that the test device construction, particularly the lateral stiffness of the compression platen, has on the resultant mechanical response of micrometer-scale compression samples that are oriented for single slip deformation. We compare the observed experimental results to those obtained by anisotropic crystal plasticity FEM simulations [25] of similar test structures in order to better understand the influence of the test boundary conditions on the uniformity of the internal stress state.

2. Procedure

2.1. Device Construction

As mentioned in the introduction, we have constructed an in-situ testing device to carry out mechanical tests on micrometer-scale specimens within the SEM. Figure 1 presents a schematic illustration of the test frame that can be placed on the stage of an SEM microscope. A CEDRAT parallel pre-stressed piezoelectric actuator is used to impose sample displacements, which provides sub-nanometer displacement control in both tension and compression over a total stroke of 40 micrometers. An alignment flexure is employed to ensure completely axial motion of the load train [26,27]. A traditional strain-gage based load cell is used to measure the force applied to the sample. The range and sensitivity of the load cell used in this study is 100 and 0.05 grams respectively. As Figure 1 illustrates, the compression platen is attached to the end of the load cell. At the other end of the test device, an Attocube Systems piezoelectric controlled slip-stick motion x-y-z positioning stage is used to precisely place the microcrystals underneath the compression platen. This stage bases its movement on a piezoelectric inertial force mechanism that provides nanometer scale positioning resolution with zero backlash.

Importantly, this setup allows for the exchange of various compression platens. This has allowed us to explore whether the relative ease of translation of the loading axis in certain commercial nanoindentation systems effectively acts to lower the platen-sample friction coefficient [3], mimicking a well lubricated macro-scale compression experiment. In the present report, compression platens composed of a diamond crystal and a SiC fiber have been evaluated and compared. A conical diamond platen was purchased from Micro Star Technologies; it is 1 millimeters long and 0.5 millimeters wide at one end, tapering to a flat surface that is 40 by 40 micrometers in area at the other end. A second tip was manufactured from a SiC fiber, which measured 8 millimeters in length by 0.1 millimeters in diameter. A flat contact surface was prepared by polishing with a dimpling device and subsequent FIB milling. The 80:1 aspect ratio of the SiC fiber enables the lateral stiffness of this loading platen to be extremely low.

The lateral stiffness of both the diamond and SiC platens were measured by using a second load cell which was attached to the Attocube Systems positioning stage at one end and either the diamond or SiC compression platen at the other. The Attocube Systems stage was used to laterally drive the implemented compression platen, and the resultant forces and displacements were measured using the second load cell and SEM images respectively. From these measurements, the calculated stiffness of the SiC platen was determined to be less than 0.0001 Newtons per micrometer of lateral translation, and that of the diamond platen to be 0.1 Newtons per micrometer.

The microcrystals examined in this study have been machined at the edge of a bulk sample. This geometry allows for imaging of microcrystals during deformation from an orientation perpendicular to the loading axis. Tests are conducted in a quasi-static manner, where samples undergo sequential periods of loading at a constant voltage ramp rate (open-loop displacement-rate control), separated by periods where the piezoelectric actuator is held at a constant voltage in order to optimize the collection of high-resolution SEM images. The strain rate during the loading periods was

approximately 10^{-4} s^{-1}. The dimensions of the images recorded in this study were 4096 by 2048 pixels, with a corresponding pixel size of 7.5 nanometers. The entire process of performing the mechanical test and collecting SEM image data was automated using custom scripts written in LabView.

Following completion of the experiment, the sample displacements were calculated directly from the image data by tracking the motion of distinct features that were FIB-milled into the sample surface (see Figure 2). This feature tracking was accomplished using a custom script written in IDL which calculated the motion of each target feature to sub-pixel resolution. These displacements were correlated with load data collected throughout the experiment, and were subsequently used to construct load-displacement and stress-strain curves.

2.2. Experiments

The material examined in this work is Rene N5, a single crystal Ni base superalloy commonly used in turbine blade applications [28]. The back-reflection Laue method was used to orient a bulk sample for a $[\bar{1}23]$ single slip compression axis. Further, the sample was oriented such that the viewing direction during testing was parallel to the $[1\bar{1}1]$ direction, which placed the primary slip system's Burgers vector $[\bar{1}01]$ entirely within the imaging plane. Compression samples were fabricated using a two step process, first by micro-electrodischarge machining (micro-EDM) using a Sarix SX-100 followed by a FIB-based 'lathe' milling procedure [2]. FIB milling was performed using either a FEI Nova 600 or FEI DB235 FIB-SEM, where the ion accelerating voltage was 30 kV. All samples in this study were nominally 10 micrometers in diameter with a 2.3:1 gage length-to-diameter aspect ratio. Prior to testing, the top surface of each sample was FIB milled parallel to the face of the compression platen to minimize contact misfit. After testing, internal lattice rotations were measured in selected deformed samples by preparing a cross-section surface using standard FIB milling procedures, and subsequently collecting EBSD patterns using a TSL OIM system attached to a FEI XL30 SEM. The pixel size of the corresponding EBSD maps was 50 nanometers.

2.3. Simulations

An anisotropic crystal plasticity FEM model was implemented using the commercial FEM program ABAQUS, in order to better understand the effect of the test boundary conditions on the in-situ SEM compression experiments. Selected details of these simulations have been reported previously [25]. The simulations were conducted with a $[\bar{1}23]$ sample orientation and boundary conditions that mimicked the experiments. In order to model the lateral constraint of the test system, a Coulomb friction coefficient was ascribed to the sample-platen interface. A value of 0.0 allows for the top of the sample to move fully unconstrained, while a value of 1.0 corresponds to perfect friction where the top of the sample is constrained to move only in the direction of the compression axis. These extreme values were used to approximate the constraints

imposed when implementing the SiC fiber and diamond compression platens respectively.

3. Results

Figure 2 shows the results from representative constrained (employing the high lateral stiffness diamond platen) and unconstrained (employing the low lateral stiffness SiC fiber platen) compression experiments. There are several differences between the two tests that are worth noting. Figure 2A shows images at various strain levels during a representative constrained experiment. Note that very fine slip traces are distributed continuously along the sample gage length. By comparison, images at various strain levels from an unconstrained experiment are shown in Figure 2B, where one can see that the majority of deformation has been localized to a few intense slip bands. This difference in the distribution of slip bands is also related to the degree of intermittency that is present in the stress-strain curves of Figure 2C. The unconstrained experimental flow curves consist of a few intermittent periods of loading that are separated by relatively large strain bursts and associated load drops. Comparatively, the constrained experiments exhibit many more strain bursts and load drops that are also much smaller in magnitude. Additionally, the constrained experiments have a positive and increasing strain hardening rate while the unconstrained experiments on average have no strain hardening (although between strain bursts the strain hardening rate is positive). Finally, we note the difference in the deformed sample geometry. The constrained sample had a barreled shape, compared to the unconstrained sample that showed no signs of barreling.

The average flow stress at 1% engineering strain for the constrained compression experiments was measured to be 1005 MPa with a standard deviation of 13 MPa, while that of the unconstrained experiments was 1042 MPa with a standard deviation of 68 MPa. In two of the unconstrained experiments the samples exhibited a strain burst before reaching 1% strain, and for those cases the stress just prior to the initiation of the burst was used to calculate the 1% flow stress. The expected bulk elastic modulus for this alloy and orientation is 240 GPa [29]. Initial loading slope values for these experiments were measured to be 282 GPa with a standard deviation of 25 GPa for the constrained tests and 228 GPa with a standard deviation of 50 GPa for the unconstrained experiments.

Figure 3 shows predicted stress-strain curves for constrained (Coulomb friction coefficient of 1.0) and unconstrained (Coulomb friction coefficient of 0.0) crystal plasticity FEM simulated compression experiments. While the FEM model does not account for deformation intermittency, it does predict a dramatic change in strain hardening rate for the two conditions. The FEM model predicts loading slope values of 253 GPa and 240 GPa for the constrained and unconstrained simulations respectively. The elastic limits for the two conditions are very similar, with a ratio of unconstrained to constrained flow stress values at 0.05% engineering strain of 1.01. The ratio of unconstrained to constrained flow stress values at 1% engineering strain is 0.94. Also included in Figure 3 are predicted deformed sample geometries at 10% engineering strain. Note that the deformed sample from the constrained experiment is barreled while that of the unconstrained experiment is not.

Figure 4 shows simulated and experimental cross-sections that plot the local disorientation relative to the original sample orientation or the orientation of the sample substrate respectively. The plane normal of the cross-section surface is $[1\bar{1}1]$, and the Burgers vector of the primary slip system $[\bar{1}01]$ lies in the plane of the page. Corresponding pole figures are shown next to the experimental plots. Figure 4 includes a key for correlating color intensity to the relative degree of disorientation and also shows a stereographic projection that denotes the microcrystal orientation relative to the directions of the pole figures. The simulated cross-sections are at 10% engineering strain while the experiments are at 11% and 8% engineering strain for the constrained and unconstrained cases respectively.

4. Discussion

4.1. Elastic Modulus and Comparison to Simulations

As mentioned in the results, the elastic modulus was experimentally measured to be 282 GPa with a standard deviation of 25 GPa for the constrained tests and 228 GPa with a standard deviation of 50 GPa for the unconstrained tests. Qualitatively, this matches the trend predicted by the FEM simulations that the constrained experiments would follow a higher measured elastic loading slope, where the simulations predict 253 GPa and 240 GPa for the constrained and unconstrained simulations respectively. The quantitative deviation in the measured experimental values is likely an indicator of variation in quality of sample alignment. As mentioned in the procedure section, the tops of the microcompression samples were FIB milled parallel to the compression platen to minimize contact misfit. While this certainly improved the fidelity of the resulting experimental data, it is not an exact procedure and any errors would easily propagate into changes in the measured loading slope values.

4.2 1% Flow Stress and Comparison to Simulations

The ratio of unconstrained to constrained flow stress values at 1% engineering strain was experimentally measured to be 1.04. This is in disagreement with the FEM predicted ratio of unconstrained to constrained flow stress values at 1% engineering strain of 0.94. The FEM simulations do predict a positive ratio of flow stress values at the elastic limit, however, which is related to an increase in stress concentration at the sample corners in the constrained simulation. In the simulations, this initially higher unconstrained flow stress is quickly overcome due to the difference in strain hardening rates for each condition. Experimentally, the enhancement in stress concentration for the constrained condition may have more significant implications regarding initiation of dislocation activity.

4.1. Strain Hardening and Comparison to Simulations

While the FEM simulations as constructed cannot account for the extreme slip localization and intermittency found in the some of the experiments, other features of the tests can be well described. Note the general similarities in observed and predicted post-test sample geometries for both the constrained (Figures 2A and 3) and unconstrained (Figures 2B and 3) cases. The constrained case exhibits significant barreling while the top of the sample in the unconstrained case is laterally-offset from the base. In fully unconstrained compression testing of a single crystal in a single-slip orientation, the upper half of the crystal is expected to offset relative to the lower half. The lateral constraints imposed by either friction at the platen-sample interface in the simulations or the stiffness of the loading platen in the experiments prevents this offset from occurring, effectively imposing a shape change on the deformed sample. This shape change is accomplished via lattice rotations and the associated activation of secondary slip systems, therefore likely imparting strain hardening.

As such, local rotation data was extracted from the FEM simulations and experimentally measured with EBSD scans. For the constrained case there is again qualitative agreement between simulation and experiment. The constrained microcrystal exhibits large bands of disoriented regions that span the width of the samples. In the experiments, the central region has rotated more than 8° from its original position, while in the simulations this rotation is 10°. This small difference can probably be accounted for by the fact that the diamond compression platen in the experiments does not provide a perfect constraint. The traces of the bands of similar disorientation are nearly perpendicular to the traces of the primary slip planes. Also note the streaking in the pole figure for the constrained experiments that is absent in the unconstrained experiments. The linear streaking in the pole figure indicates that the orientation of slip direction within the central region of the microcrystal is rotating away from the original compression axis, as expected [30]. These large rotations (and concomitant gradients) in the constrained case result in the activation of secondary slip systems and the combination of local rotations and significant activity on non-primary slip systems provides an explanation for the increase in strain hardening relative to the unconstrained case. As further evidence, Figure 5 shows predicted accumulated shear strain plots for various slip systems at 10% engineering strain for both the constrained and unconstrained simulation cases. Note the high degree of activity of the $(\bar{1}\bar{1}1)$ [011] system in the corners of the constrained simulation. While this system has a somewhat lower Schmid factor (0.29) than other available secondary systems (0.35), activity on this system acts to accommodate for the offset imposed by activity on the primary slip system (111) $[\bar{1}01]$.

In the unconstrained case, one can observe less agreement between simulation and experiment, as the experimental sample contains essentially no systematic or large bands of disoriented regions, while the simulations show qualitatively similar bands to the constrained case, but the magnitude of the disorientations are reduced considerably. As mentioned previously, one difference between the simulations and the experiments is that the FEM simulations as implemented cannot replicate the strain intermittency that dominates the experimental flow curves. These strain bursts allow for the lateral translation of the top surface of the sample without local bending of the sample, while the simulations must maintain continuity between adjacent elements and therefore some bending must occur when the top sample surface laterally-translates. Another difference is that a small band of disorientated material is observed at the outer edges of the

experimental sample, which is not observed in the simulations. The origin of these local rotations is not currently known, but may be associated with a local pile-up of dislocations at the surface. The magnitude of this disorientation is less than 0.5°. Also note the lack of activity on other slip systems for the unconstrained case in the accumulated shear strain plots of Figure 5.

4.2. Intermittency

A common attribute of microcrystal compression experiments is the observation of intermittent plastic flow, where deformation proceeds by avalanches of dislocation activity. This phenomena and its possible ties to a self-organized critical process has been discussed previously by some of the present authors [3,31,32] and others [7,9,33]. While the present results are of insufficient temporal resolution for a quantitative analysis of these events, the difference in behavior between the two different lateral constraints is dramatic. The unconstrained experiments contain a number of large displacement events, which have magnitudes that are often 500 nanometers or larger. Comparatively, similar scale events are largely absent from the constrained experiments, with the largest events typically around 150 nanometers. From these results, it is clear that the degree of imposed lateral constraints in microcompression experiments may affect the statistical distribution of displacement events, especially the magnitude of the largest events. This effect should be considered in future analyses of self-organized critical behavior.

5. Conclusions

This study presents experimental microcompression test results that have been obtained using a custom-built device that enables in-situ mechanical testing within a SEM. Initial experiments with this device demonstrate that the degree of lateral constraint of the compression platen in microcompression experiments affects many aspects of the stress-strain response, such as the flow stress, elastic modulus, strain hardening rate, dislocation intermittency, and the associated spatial distribution of displacement events, which has implications for self-organized-criticality investigations. In particular, the degree of lateral constraint had a dramatic effect on the microcrystal strain hardening behavior, and this change was confirmed by FEM simulations that closely mimic the experimental tests. This change in strain hardening behavior was linked to the activation of multiple slip systems that are largely dormant in the unconstrained experiment. This multi-slip deformation results in local lattice rotations in the constrained case that are qualitatively predicted by FEM simulations. From a practical perspective, the degree of lateral constraint in a microcompression test system can strongly influence the observed behavior and should be considered in the design and interpretation of microcrystal experiments.

Acknowledgements

The authors gratefully acknowledge A. Shiveley, A. Smith, D. Sergison, and R. Kerns for their contributions to this work. The authors acknowledge support from the Air Force Office of Scientific Research and the Materials & Manufacturing Directorate of the Air Force Research Laboratory.

References

[1] M.D. Uchic, D.M. Dimiduk, J. Florando, W.D. Nix, Science 305 (2004) 986-989.
[2] M.D. Uchic, D.M. Dimiduk, Mater. Sci. Eng. A 400-401 (2005) 268-278.
[3] D.M. Dimiduk, M.D. Uchic, T.A. Parthasarathy, Acta Mater. 53 (2005) 4065-4077.
[4] E.M. Nadgorny, D.M. Dimiduk, M.D. Uchic, Mater. Res. Soc. Symp. Proc. 976-EE06 (2007) 24-29.
[5] J.R. Greer, W.C. Oliver, W.D. Nix, Acta Mater. 53 (2005) 1821-1830.
[6] J.R. Greer, W.D. Nix, Phys. Rev. B 73 (2006) 245410-245415.
[7] S. Brinckmann, J.Y. Kim, J.R. Greer, Phys. Rev. Lett. 100 (2008) 155502.
[8] D. Kiener, C. Motz, T. Schoberl, M. Jenko, G. Dehm, Adv. Eng. Mater. 8 (2006) 1119-1125.
[9] K.S. Ng, A.H.W. Ngan, Acta Mater. 56 (2008) 1712-1720.
[10] H. Bei, S. Shim, E.P. George, M.K. Miller, E.G. Herbert, G.M. Pharr, Scripta Mater. 57 (2007) 397-400.
[11] H. Bei, S. Shim, G.M. Pharr, E.P. George, Acta Mater. (2008) In Press.
[12] C.A. Volkert, E.T. Lilleodden, Philos. Mag. 86 (2006) 5567-5579.
[13] C.P. Frick, B.G. Clark, S. Orso, A.S. Schneider, E. Arzt, Mater. Sci. Eng. A 489 (2008) 319-239.
[14] Z.W. Shan, R.K. Mishra, S.A. Syed Asif, O.L. Warren, A.M. Minor, Nature Mater. 7 (2008) 115-119.
[15] M.D. Uchic, D.M. Dimiduk, R. Wheeler, P.A. Shade, H.L. Fraser, Scripta Mater. 54 (2006) 759-764.
[16] G.I. Taylor, W.S. Farren, Proc. Roy. Soc. A 111 (1926) 529-551.
[17] E 9 – 89a Standard Test Methods of Compression Testing of Metallic Materials at Room Temperature
[18] D.H. Lassila, M.M. LeBlanc, G.J. Kay, J. Eng. Mater. Technol. – Trans. ASME 124 (2002) 290-296.
[19] D.H. Lassila, M.M. LeBlanc, J.N. Florando, Metall. Mater. Trans. A 38 (2007) 2024-2032.
[20] H. Zhang, B.E. Schuster, Q. Wei, K.T. Ramesh, Scripta Mater. 54 (2006) 181-186.
[21] D. Raabe, D. Ma, F. Roters, Acta Mater. 55 (2007) 4567-4583.
[22] D. Kiener, C. Motz, G. Dehm, J. Mater. Sci. 43 (2008) 2503-2506.
[23] R. Maass, S. Van Petegem, D. Grolimund, H. Van Swygenhoven, D. Kiener, G. Gehm, Appl. Phys. Lett. 92 (2008) 071905.
[24] A.S. Budiman, S.M. Han, J.R. Greer, N. Tamura, J.R. Patel, W.D. Nix, Acta Mater. 56 (2008) 602-608.

[25] Y.S. Choi, M.D. Uchic, T.A. Parthasarathy, D.M. Dimiduk, Scripta Mater. 57 (2007) 849-852.
[26] R.V. Jones, J. Sci. Instrum. 28 (1951) 38-41.
[27] R.V. Jones, J. Sci. Instrum. 33 (1956) 11-15.
[28] P. Caron, T. Khan, Aereosp. Sci. Tech. 3 (1999) 513-523.
[29] J. Rigney, GE Aviation. Personal Communication 10 Oct. 2006.
[30] G.I. Taylor. Proc. Roy. Soc. A 116 (1927) 16-38.
[31] D.M. Dimiduk, C. Woodward, R. LeSar, M.D. Uchic, Science 312 (2006) 1188-1190.
[32] D.M. Dimiduk, M.D. Uchic, S.I. Rao, C. Woodward, T.A. Parthasarathy, Model. Simul. Mater. Sci. Eng. 15 (2007) 135-146.
[33] F.F. Csikor, C. Motz, D. Weygand, M. Zaiser, S. Zapperi, Science 318 (2007) 251-254.

Figure Captions

Figure 1: Schematic illustration of the in-situ microtest frame used in these experiments. See text for details.

Figure 2: Compression experiments on Rene N5 microcrystals with a $[\bar{1}23]$ compression axis and 10 micrometer diameters. (A) Three SEM images at various strain levels while employing a high lateral stiffness diamond platen. (B) Three SEM images at various strain levels while employing a low lateral stiffness SiC platen. (C) Corresponding stress-strain curves.

Figure 3: Crystal plasticity FEM simulated flow curves for a $[\bar{1}23]$ oriented nickel base superalloy in compression. The unconstrained condition corresponds to a Coulomb friction coefficient of 0.0 at the sample-platen interface while the constrained condition corresponds to a Coulomb friction coefficient of 1.0. The inset deformed sample geometries are for 10% engineering strain.

Figure 4: Disorientation maps for simulated and experimental $[\bar{1}23]$ oriented microcompression tests, which examine either the constrained or unconstrained platen condition. The arrow on each figure represents the direction of the Burgers vector of the primary slip system $[\bar{1}01]$, which lies in the plane of the map. The viewing direction is $[1\bar{1}1]$.

Figure 5: Predicted accumulated plastic shear strain maps at the compression sample center at 10% engineering strain for the simulations shown in Figure 3. The four most active slip systems are shown and the viewing direction is $[1\bar{1}1]$.

ks

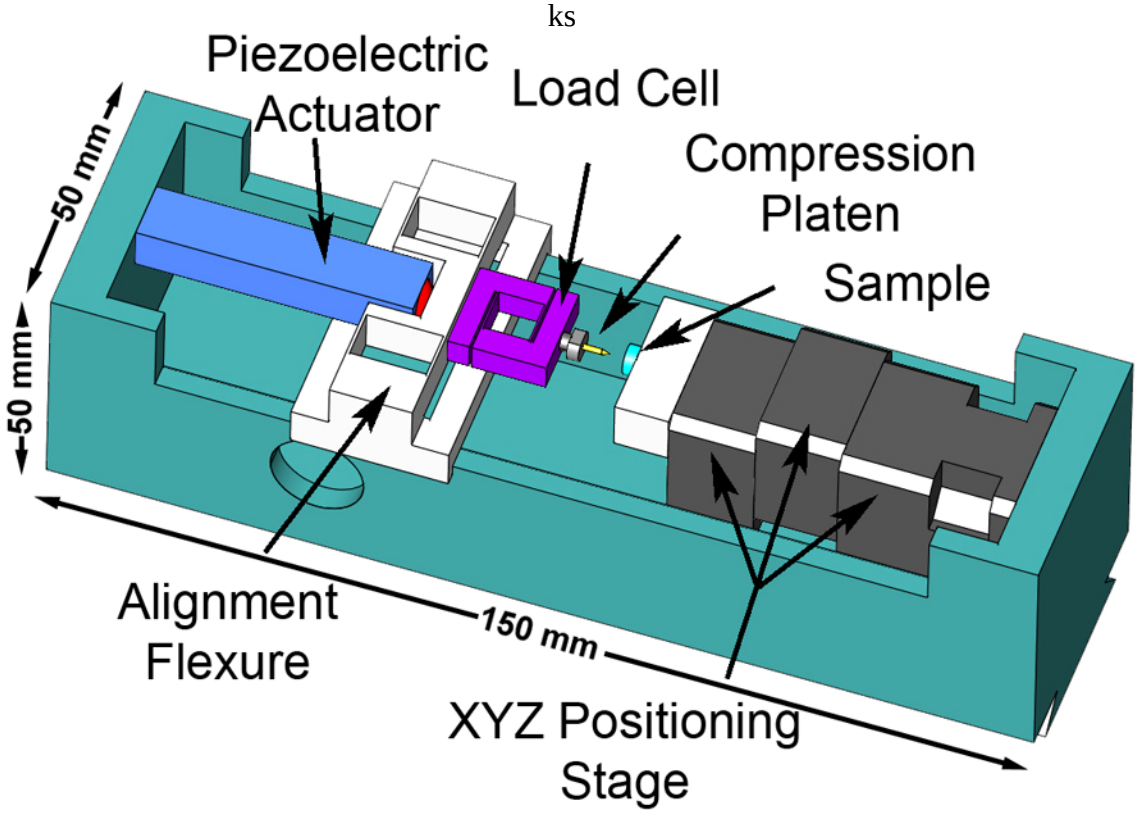

Figure 1: Schematic illustration of the in-situ microtest frame used in these experiments. See text for details.

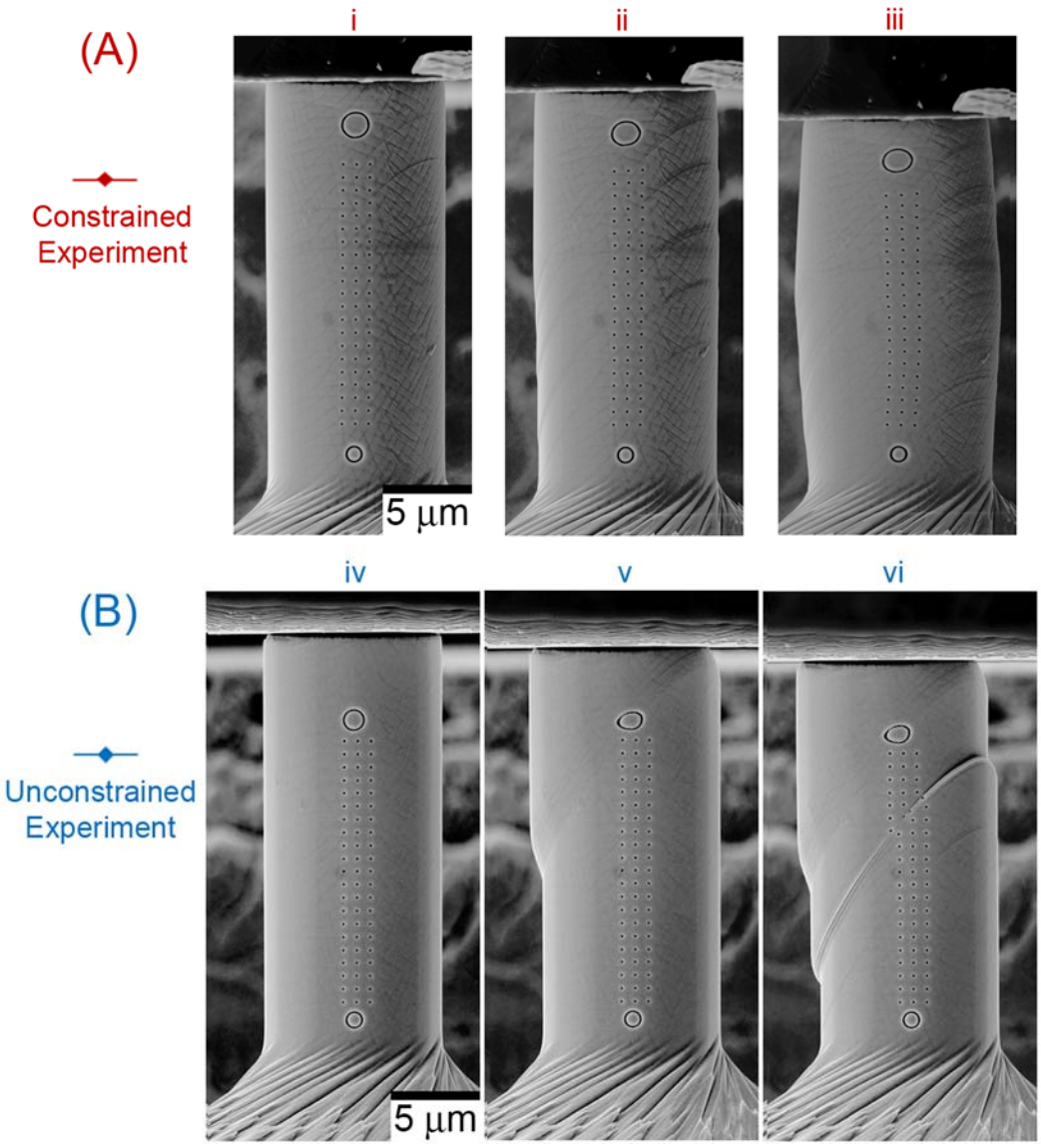
(A)
i
ii
iii
Constrained
Experiment
5 μm
(B)
iv
v
vi
Unconstrained
Experiment
5 μm

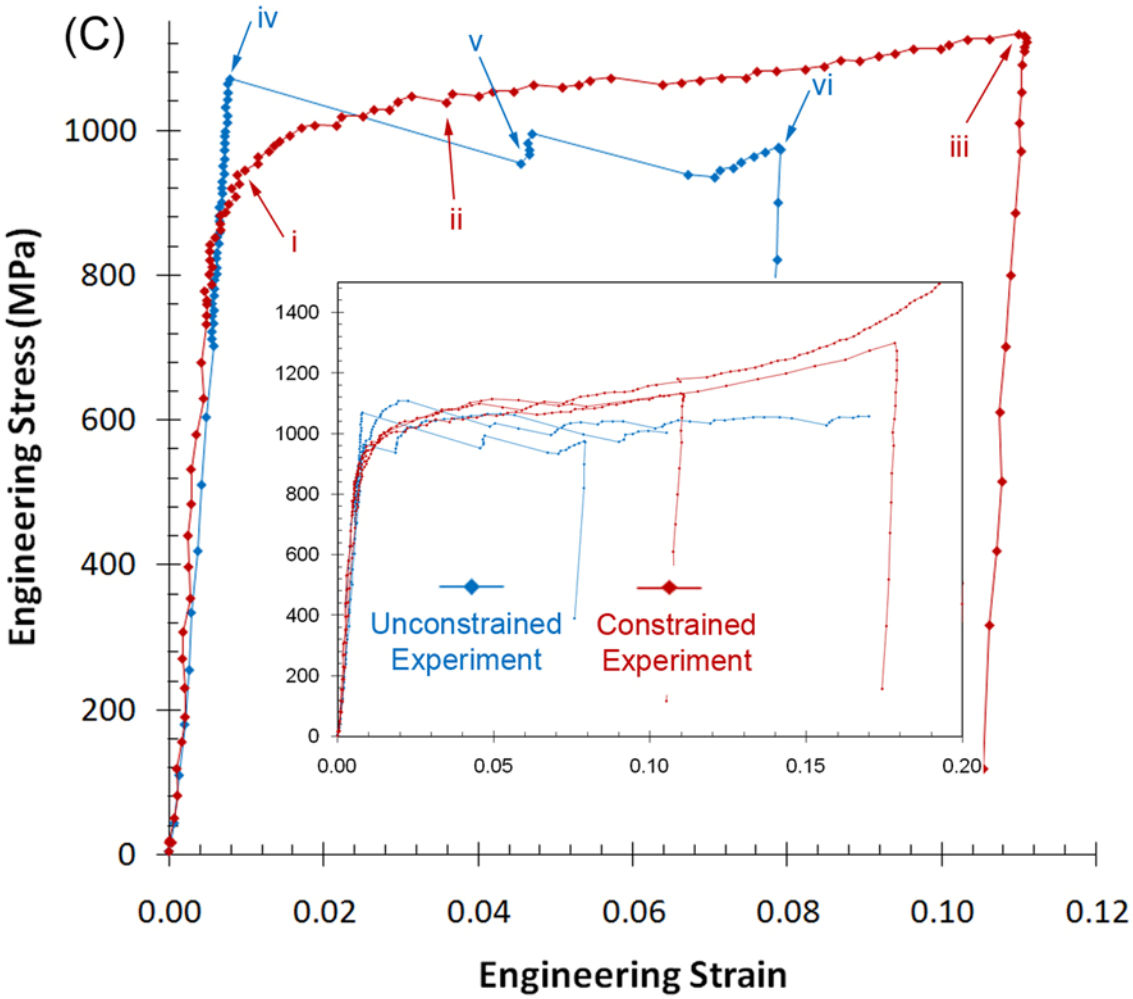

Figure 2: Compression experiments on Rene N5 microcrystals with a $[\bar{1}23]$ compression axis and 10 micrometer diameters. (A) Three SEM images at various strain levels while employing a high lateral stiffness diamond platen. (B) Three SEM images at various strain levels while employing a low lateral stiffness SiC platen. (C) Corresponding stress-strain curves.

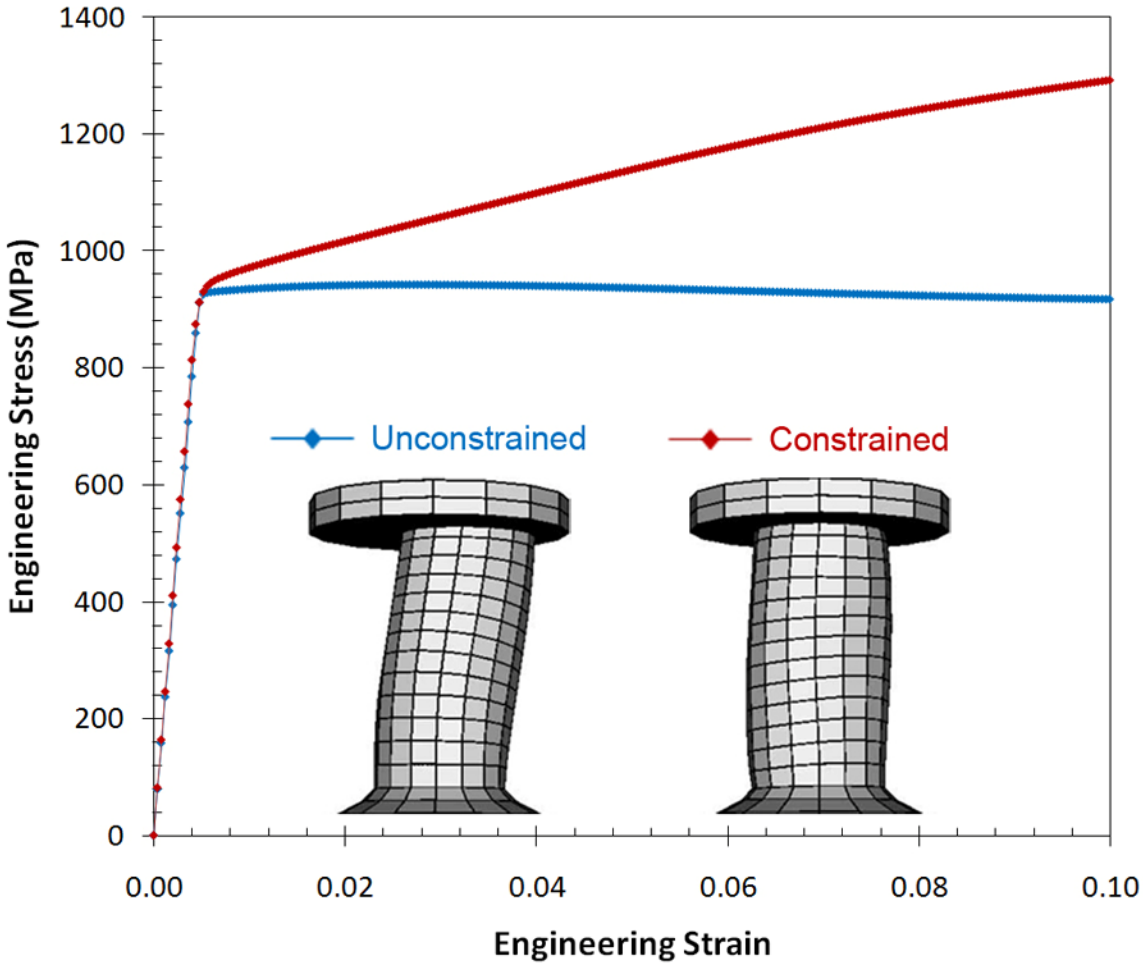

Figure 3: Crystal plasticity FEM simulated flow curves for a $[\bar{1}23]$ oriented nickel base superalloy in compression. The unconstrained condition corresponds to a Coulomb friction coefficient of 0.0 at the sample-platen interface while the constrained condition corresponds to a Coulomb friction coefficient of 1.0. The inset deformed sample geometries are for 10% engineering strain.

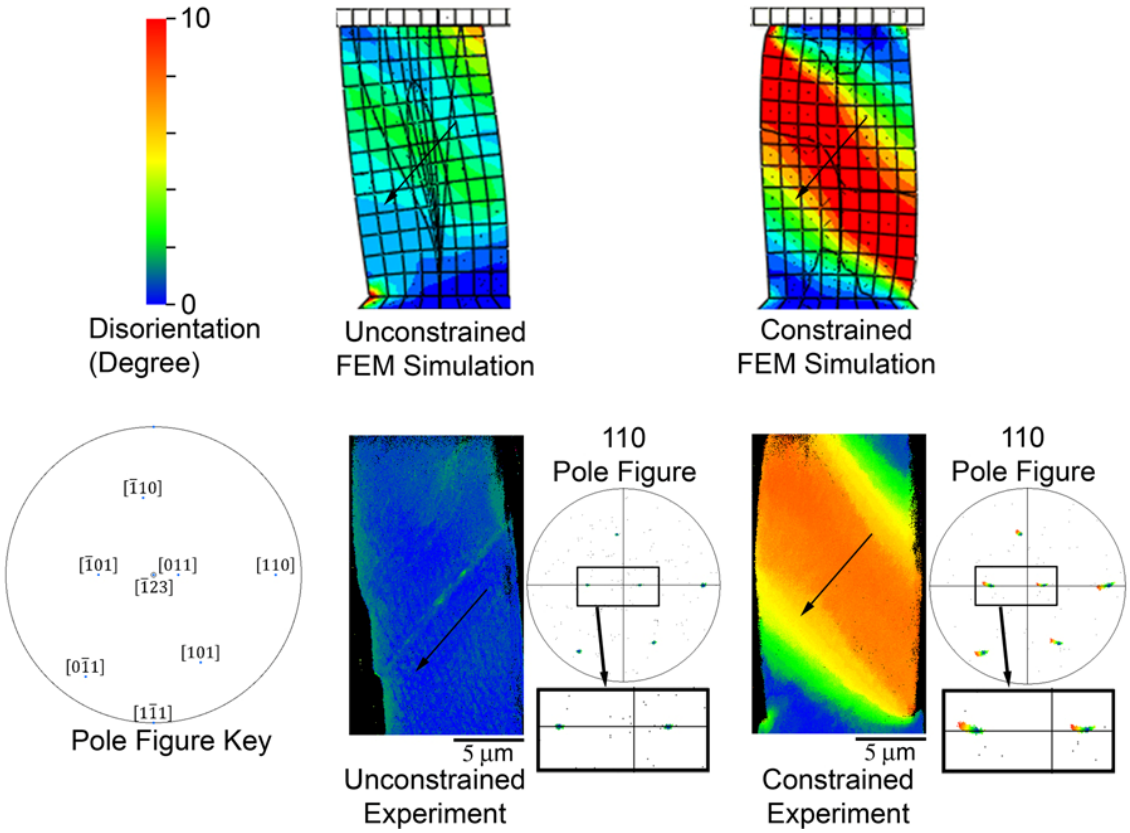

Figure 4: Disorientation maps for simulated and experimental [$\bar{1}$23] oriented microcompression tests, which examine either the constrained or unconstrained platen condition. The arrow on each figure represents the direction of the Burgers vector of the primary slip system [$\bar{1}$01], which lies in the plane of the map. The viewing direction is [1$\bar{1}$1].

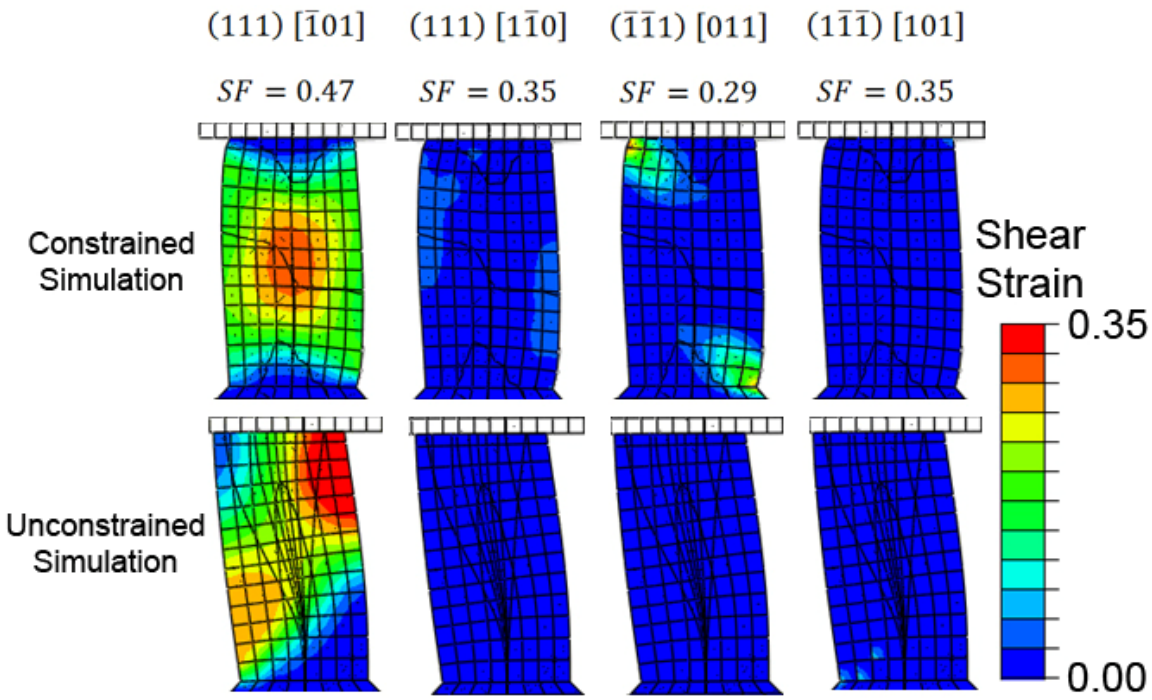

Figure 5: Predicted accumulated plastic shear strain maps at the compression sample center at 10% engineering strain for the simulations shown in Figure 3. The four most active slip systems are shown and the viewing direction is [1$\bar{1}$1].